Electron beam induced current and cathodoluminescence study of proton irradiated $InAs_xP_{1-x}$/InP quantum-well solar cells

Robert J. Walters[a] and G. P. Summers
U.S. Naval Research Laboratory, Code 6825, Solid State Devices Branch, 4555 Overlook Ave., S.W., Washington, DC 20375

S. R. Messenger
SFA, Inc., Largo, Maryland 20774

M. J. Romero and M. M. Al-Jassim
National Renewable Energy Laboratory, 1617 Cole Boulevard, Golden, Colorado 80401-3393

R. Garcia and D. Araujo
Universidad de Cadiz, Apdo. 40, E-1150, Puerto Real (Cadiz), Spain

A. Freundlich, F. Newman, and M. F. Vilela
Space Vacuum Epitaxy Center, University of Houston, Houston, Texas 77240

(Received 12 December 2000; accepted for publication 25 May 2001)

The effects of proton irradiation on strained $InAs_xP_{1-x}$/InP-based quantum well solar cells (QWSCs) have been investigated by the electron beam induced current (EBIC) and cathodoluminescence (CL) techniques. From analysis of the EBIC data, capture rates within the quantum well region have been estimated, from which the open circuit voltages of the cells were calculated and shown to agree well with the measured values. Diffusion lengths have been estimated from analysis of both the EBIC and CL measurements. The location of the energy levels of proton-induced defects and their effectiveness as nonradiative recombination centers have been determined from Arrhenius plots of the total CL intensity emitted from the quantum wells following irradiation. The results suggest that deeper and narrower quantum wells increase the sensitivity of QWSCs to radiation damage. © *2001 American Institute of Physics.* [DOI: 10.1063/1.1389755]

I. INTRODUCTION

The US Naval Research Laboratory (NRL) and the University of Houston (UH) have been collaborating on the development of quantum well solar cells (QWSCs) for space applications. The initial focus of this research has been to develop a high-efficiency, radiation-resistant solar cell by incorporating a multiquantum-well (MQW) layer within the depletion region of an InP solar cell grown heteroepitaxially on a Si substrate. The radiation resistance of InP solar cells is well known,[1] as are the advantages of an InP solar cell grown on lightweight, robust Si wafers for space applications.[2] However, the beginning-of-life efficiencies of InP/Si solar cells grown to date have been relatively low as a result of the effects of defects introduced by the lattice mismatch between InP and Si. The goal of the present research is to offset this performance degradation by exploiting the efficiency increase provided by the incorporation of MQWs within the device structure.[3] The strained-layer, $InAs_xP_{1-x}$/InP MQW system was chosen for study because of the potentially high efficiency enhancement predicted by Anderson's ideal theory of QWSCs.[4]

NRL also has an ongoing research collaboration with the University of Cadiz (UCA) aimed at applying the techniques of electron beam induced current (EBIC) and cathodoluminescence (CL) to the study of the effects of defects in solar cells. Recently, the collaborative efforts between NRL, UH, and UCA have been combined in order to study carrier transport behavior in the MQW region of $InAs_xP_{1-x}$/InP QWSCs before and after proton irradiation. The results have been incorporated into Anderson's ideal theory to quantify the effect of MQW structures on solar cell radiation response. This article reports results from this research.

II. EXPERIMENTAL DETAILS

The QWSCs used in these studies were single junction InP structures, in which a ten period, strained-layer $InAs_xP_{1-x}$/InP MQW region was incorporated in the depletion region between the emitter and the base (Fig. 1). The cells were grown by chemical beam epitaxy at 510 °C on S-doped InP (001) substrates. Details of the fabrication have been described previously.[5] Table I shows some structural parameters of the QWSCs, where the photoluminescence energy corresponds to the MQW emission at 10 K.[6]

The solar cells were irradiated through the front surface with monoenergetic, normal incidence 3 MeV protons using the Pelletron Accelerator facility at the Naval Surface Warfare Center at White Oak, Maryland. The fluences were determined from the total charge striking the target plane using a current integrator. The accuracy of the dosimetry in all cases was estimated to be about 10%.

For EBIC and CL measurements, the QWSCs were observed in the (001) direction on to cleaved {110} surfaces,

[a]Electronic mail: rwalters@ccf.nrl.navy.mil

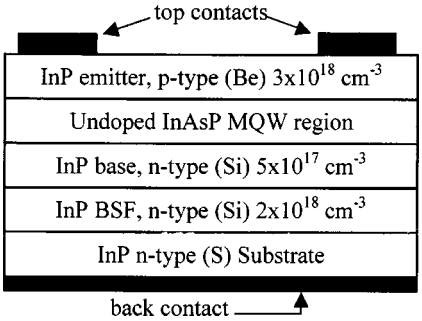

FIG. 1. Schematic diagram of the InP-based QWSCs. These are strained $InAs_xP_{1-x}$/InP layers. Details are given in Table I.

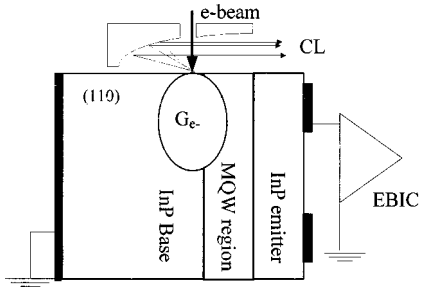

FIG. 2. Configuration of the EBIC and CL measurements made on a JEOL-JSM820 scanning electron microscope. The electron beam was incident on a freshly cleaved {110} face, oriented perpendicular to the growth direction of the MQW.

which were perpendicular to the MQW (Fig. 2). Prior to loading into the scanning electron microscope, they were mounted on a holder that had been modified so that pressure could be applied to the top and back contacts. The EBIC was detected using a head amplifier and a low input-impedance Matelect ISM5A amplifier. The incident electron beam current was measured by a Faraday cup.

A semiparabolic mirror attached to an optical guide yielded highly efficient collection of the CL excited by the e-beam. Spectroscopic measurements were made using a cryogenically cooled charge coupled device (Photometrics SDS9000) attached to a modified Oriel 77400 spectrograph. The cells were typically cooled to 60 K during the CL measurements. Since the cell arrangement was the same during the EBIC and CL measurements, both signals can be recorded simultaneously.

III. EXPERIMENTAL RESULTS

A. EBIC signal saturation regime

Prior to irradiation, the current saturation regime of the QWSCs was investigated by imaging the EBIC at different bias and excitation levels. The saturation regime is attained when 100% of the carriers generated within the MQW region are collected. This condition can be determined from analysis of the EBIC signal. When the diffusion of carriers is restricted by capture in the MQW region, a reduction of the EBIC signal is observed. Under these conditions, the usual assumption of 100% collection efficiency cannot be made. Away from the saturation regime, a detailed analysis of the signal as described in the Appendix leads to an estimate of the carrier capture lifetime, τ_{cap}, in the MQW region. Figure 3 illustrates the results of this analysis for QWSC UH716, which is representative of the cells studied. At zero applied bias, the intrinsic region acts as a perfect collector at electron beam currents above ~500 pA, which corresponds to an excess carrier density of $\sim 10^{17}$ cm^{-3}. At a lower excitation level (150 pA), there is a reduction of the signal in the MQW region, thus, the saturation regime is not attained. The effect of biasing is, in general, to change the excitation level at which saturation occurs. An increase in the forward bias, which causes a decrease in the internal MQW electric field, results in an increase in the excitation level required to saturate the signal. The inverse is true when a reverse bias is applied.

The results of Fig. 3 show the carrier collection within the MQW region to be asymmetric in the unsaturated regime. At the interface between the *n*-type base and the intrinsic region, carrier extraction is complete, but between the *p*-type emitter and the intrinsic region, it is not. Nelsen *et al.* have presented an excellent model for the transport and recombination of charge carriers in quantum well devices in Ref. 7. Within, this model, the asymmetry of the EBIC signal is interpreted as a significant background doping in the intrinsic region. The shift of the EBIC peak towards the *n*-type base region suggests *p*-type doping, since in that case, the junction electric field would not extend through the quantum wells at

TABLE I. Structural parameters of the strained $InAs_xP_{1-x}$/InP MQW solar cells studied here. The PL energy was measured at 10 K and represents the effective band gap of the well.

Cell ID	PL energy (eV)	Well width (Å)	Arsenic fraction	MQW region thickness (μm)
672	1.250	18	0.37	0.33
711	1.210	12	0.65	0.33
708	1.200	12	0.66	0.23
716	1.180	31	0.32	0.33
718	1.125	20	0.53	0.35

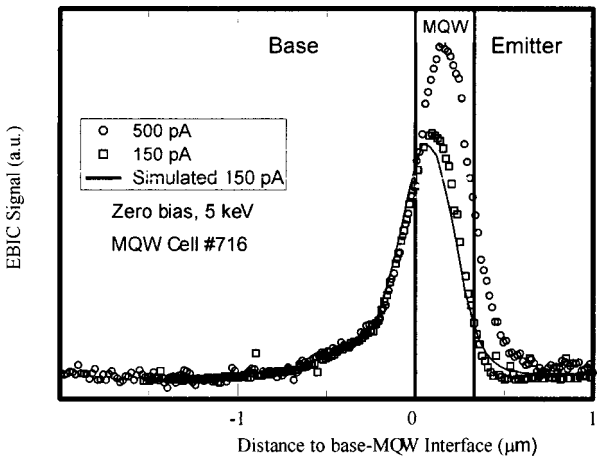

FIG. 3. EBIC line scans recorded under the two different excitation levels noted in the legend for the QWSC UH716. Increasing the electron beam current causes the signal to saturate. The solid curve represents simulated data from which the MQW capture lifetime (τ_{cap}) is estimated.

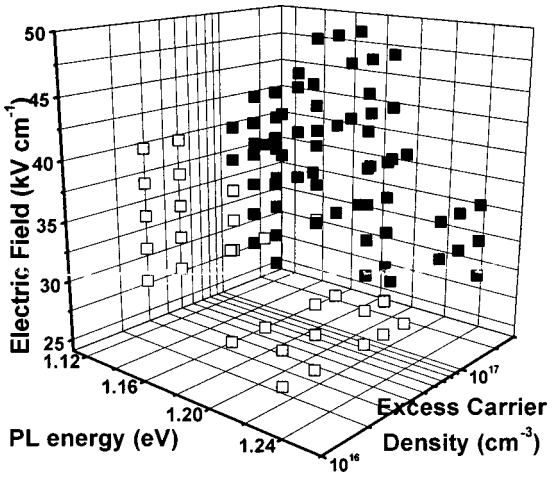

FIG. 4. Three-dimensional plot of the saturation regime at different excitonic transition energies as given by the PL peak energy measured at 10 K, electric fields (i.e., applied biases), and excess carrier densities (i.e., electron-beam current levels). A solid square represents when the EBIC is saturated (100% carrier collection within the MQW) and an open square when the EBIC is not saturated (<100% carrier collection within the MQW). Two regimes emerge, corresponding to saturation, top right, and lack of saturation, bottom right.

the emitter/intrinsic region interface. The excitation level for saturation suggests a doping level is on the order of 10^{16} cm^{-3}.

The results of repeating the analysis of the EBIC saturation regime for QWSCs with various structures are summarized in the three-dimensional plot shown in Fig. 4. Figure 4 shows the saturation regime at different excitonic transition energies as given by the photoluminescence (PL) peak energy measured at 10 K (Table I), different excess carrier densities excited by the electron beam current, and different electric fields produced by the applied biases. The excitonic transition is an internal parameter of the cell that depends on the As composition and the width of the wells and barriers. In Fig. 4, solid squares indicate saturation of the EBIC signal, and open squares indicated an unsaturated signal. The data can be seen to fall into two separate regimes corresponding to saturated conditions (top right corner), and unsaturated conditions (bottom left corner). These two regimes have to be taken into account when optimizing the design of a QWSC. As discussed by Serdiukova *et al.*,[6] a critical built-in electric field exists for optimum carrier collection within QWSCs. Using the results shown in Fig. 4 for the saturated/unsaturated boundary regions, the minimum built-in electric field can be determined for different excitonic transition energies and excitation levels. The excitation level dependence is an important parameter in optimizing a QWSC for a particular solar intensity. Indeed, a QWSC optimized for carrier collection at one sun illumination might become nonoptimized if the solar intensity drops as, in fact, happens during every orbit of a low-Earth-orbit satellite.

In EBIC experiments, the e-beam excites electron-hole pairs in both the wells and the barriers. A decrease in the EBIC would be observed if the recombination rate was high in the MQW region. However, such a decrease is not observed in the QWSCs studied here. Thus, it seems that the mechanism governing carrier reduction is the capture of excess carriers in the MQW region instead of recombination in the wells. In the rate equations shown in the Appendix, the capture lifetime is representative of the capture rate within the intrinsic region. Using the modeling approach developed at UCA,[8] the experimental data measured in the unsaturated regime have been fitted with τ_{cap} as a free parameter. The solid line in Fig. 3 shows the results of such a procedure to fit the experimental data for QWSC UH716. For all the QWSCs cells studied here, τ_{cap} was found to lie in the range 10 ps–1 ns. The capture of carriers at the MQW region, which restricts diffusion across the intrinsic region between the emitter and base, can be viewed as a reduced mobility. Since the mobility is a more convenient parameter to incorporate into Anderson's theory, an effective mobility in the intrinsic region has been estimated from the capture lifetimes using the relationship between the diffusion length L, the mobility μ, and the lifetime, τ ($L^2=\mu kT\tau/q$). For cells UH716 and UH718 in particular, at an excitation level equivalent to one sun AM0 illumination, the lifetimes correspond to effective mobilities of 20 and 30 cm^2/V s, respectively. These values will be used in the calculations to follow.

B. Open circuit voltage analysis

According to Anderson's theory,[4] and considering only radiative recombination in the unity quantum-efficiency limit, the open-circuit voltage for a QWSC can be related to that of a base line cell (i.e., a cell grown without a MQW region) by

$$V_{\mathrm{oc(QW)}}=\frac{kT}{q}\ln\left[\frac{r_G J_{\mathrm{scB}}}{J_0(1+r_R\beta)}\right], \tag{1}$$

where J_{scB} is the short-circuit current density of the baseline cell, J_0 is the reverse saturation current density, βJ_0 is the contribution to the reverse saturation current from thermal generation and radiative recombination in the intrinsic region, and kT/q is the thermal voltage. The quantity $r_G J_{\mathrm{scB}}$ is the photocurrent of the QWSC while the quantity $J_0(1+r_R\beta)$ is the QWSC reverse saturation current. It should be noted that this is essentially Anderson's Eq. (24c)[3] except that the "+1" term within the argument of the logarithm function has been ignored. This is a valid approximation since the ratio of the photocurrent to reverse saturation current is expected to be much larger than unity. The quantity r_G is the generation enhancement ratio, defined as the fractional increase in the carrier generation rate due to the incorporation of the MQW. The factor r_R is the radiative recombination enhancement ratio, which represents the fractional increase in the net intrinsic-region recombination rate due to the presence of the QWs. As required by detailed balance, r_R is expressed by

$$r_R=1+f_W[\gamma_B\gamma_{\mathrm{DOS}}^2\exp(\Delta E/kT)-1]. \tag{2}$$

In Eq. (2), f_W is the fraction of the depletion region occupied by quantum wells and ΔE is the difference in band gap energy between the InP barrier and InAsP well. The γ_B term is the "oscillator enhancement factor" given by the ratio of the recombination coefficient in the well to that in

TABLE II. Calculation of the V_{oc} for the QWSCs using Eq. (3) compared to the experimental values. The experimental values were measured under 1 sun, AM0 simulated solar light conditions. In the fourth column, V_{oc} is calculated assuming the carrier mobility of the base line InP cell ($\mu = 1500$ cm^2/V s). For the cells with more shallow wells that showed saturation at zero bias, reasonable agreement is observed. For the cells with deeper wells that did not show saturation, better agreement when V_{oc} is calculated using the effective MQW mobility (data given in column 5) as determined fits of the EBIC signal (Fig. 5).

Cell ID	ΔE (meV)	f_W	V_{oc}(V) exp.	V_{oc}(V) Calc. Eq. (3)	V_{oc}(V) Calc. Eq. (3) w/carrier capture	Saturation at zero bias?
672	171	0.05	0.73	0.74	···	Yes
711	211	0.04	0.71	0.73	···	Yes
708	221	0.05	0.70	0.73	···	Yes
716	241	0.09	0.61	0.69	0.64	No
718	296	0.06	0.61	0.65	0.60	No

the barrier. The γ_{DOS} term is the density of states (DOS) enhancement factor given by the ratio of the effect volume DOS in the well to that in the barrier. Equation (1) can be written as

$$V_{oc} = V_{ocB} + \frac{kT}{q}[\ln r_G - \ln(1 + r_R\beta)], \tag{3}$$

where V_{ocB} refers to the open-circuit voltage for an InP base line cell, which is taken to be 0.75 V.[9,10] Anderson shows that the parameter β can be expressed as

$$\beta = \sqrt{\frac{qNB_B}{4kT\mu}}W, \tag{4}$$

where W is the depletion width, B_B is the radiative recombination coefficient in the barrier (for InP, $B_B = 10^{-10}$ cm^3/s), and N is the effective doping concentration, $\sim 10^{17}$ cm^{-3}. The mobility, μ, for the base line cell is taken as 1500 cm^2/V s. Using this value of μ, V_{oc} was calculated for the MQW cells, and the results are given in Table II. The ΔE values given in Table II were determined from the PL energy data taken at 10 K (Table I) and extrapolated to 300 K.[11] The experimental values for V_{oc} of the QWSCs were determined from photovoltaic measurements made on the cells under simulated, 1 sun, AM0 solar illumination.[10]

For the QWSCs that exhibited saturation at zero bias, the V_{oc} values calculated using the mobility of a base line cell match the measured values reasonably well. However, the remaining two devices, namely UH716 and UH718, did not exhibit saturation at zero bias, suggesting significant carrier capture within the relatively deep wells. Noting that a higher capture rate can be understood as a decrease in the effective carrier mobility within the depletion region, V_{oc} was recalculated for these cells using the effective mobilities determined above from the capture lifetime at the MQW region (τ_{cap}). Using these values for the mobilities, much better fits to the experimental values of V_{oc} are obtained (Table II).

C. Effects of proton irradiation on the EBIC signal

The effects of irradiation on the EBIC signal from cells UH711 and UH672 are shown in Fig. 5. Fits of the EBIC signal collected from the base region yield an estimate of the base minority carrier (hole) diffusion length, L. For cell UH711, prior to irradiation, L is estimated to be 0.42 μm. After 3 MeV proton irradiation up to a fluence of 4×10^{13} cm^{-2}, L was degraded to $\sim$0.08 μm. For cell UH672, the base diffusion length before and after irradiation were estimated to be 0.35 and 0.10 μm, respectively. The degradation of the EBIC signal from the MQW region at the emitter/MQW region interface is understood to occur as a

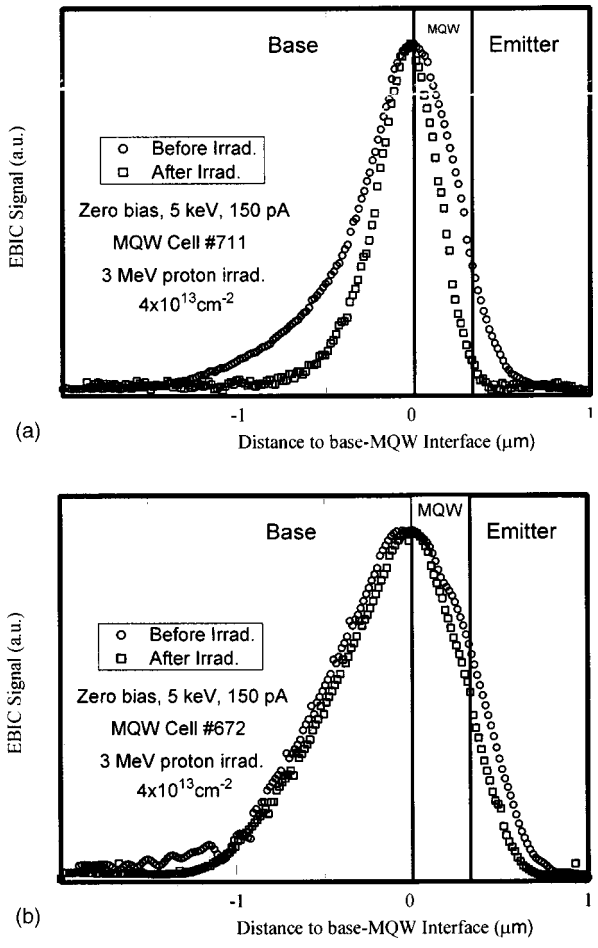

FIG. 5. Effect of proton irradiation on the EBIC linescans recorded from QWSC UH711 (a) and UH672 (b) (e-beam energy and current of 5 keV and 150 pA, respectively) at zero applied bias. Within the base, the decrease of the EBIC signal is associated with diffusion length degradation. Within the depletion region, the reduction in collection efficiency is attributed to increased carrier capture and recombination in the MQW region due to radiation-induced defect levels.

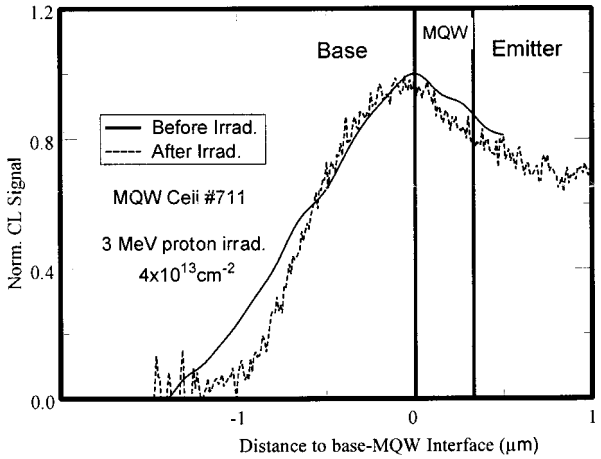

FIG. 6. Effect of proton irradiation on CL line scans measured in QWSC UH711. Analysis of these data enables an estimate of the degradation in both the base and MQW regions.

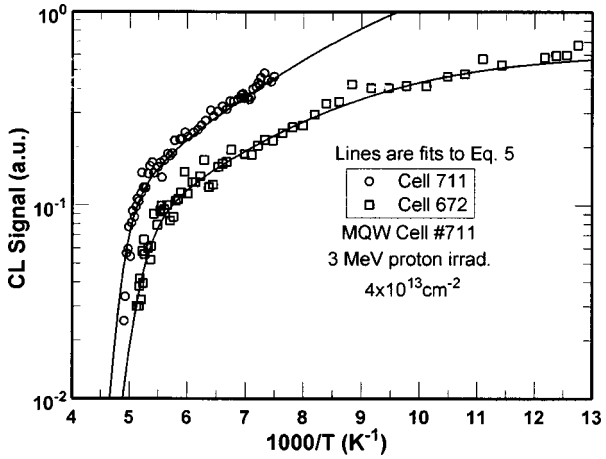

FIG. 7. Arrhenius plots of the total integrated CL signal emitted from cells UH711 and UH672 after irradiation. The solid lines are fits of the data to Eq. (5). The data reveal three thermally activated recombination channels, and the data fits yielded estimates of the defect parameters (Table III).

result of an increase in carrier capture and recombination caused by radiation-induced defects acting as recombination centers. The slightly greater degradation observed in cell UH711 may suggest increased radiation sensitivity for cells with higher As content and deeper wells. However, this may also be attributed to the thinner wells of cell UH711 as will be discussed further in Sec. IV.

D. Effects of proton irradiation on the CL signal

Linescans of the CL emitted from the quantum wells were recorded at various temperatures. Figure 6 shows the effect of proton irradiation on room-temperature line scans for the QWSC UH711. The decay of the signal far from the wells gives an estimate of the diffusion length of carriers as they recombine radiatively in the QWs (L_r). This parameter should be dependent both on the base diffusion length and the radiative recombination rate in the quantum wells, with the latter also being dependent on the injection level. The base diffusion length degradation coefficient has been found to be similar in all the QWSCs studied here, so any differences observed amongst the cells are attributed to the radiation-induced changes in the QW recombination rate. For cell UH711, fits of the experimental data produced an estimate of L_r of 0.55 μm prior to irradiation and 0.16 μm afterwards. For cell UH672, with similar structural parameters to UH711 but with lower As content and thus shallower wells, L_r was determined to be 0.40 and 0.22 μm before and after irradiation, respectively. These results again suggest that deeper wells may result in increased cell radiation sensitivity.

Figure 7 shows Arrhenius plots of the total integrated CL signal intensity from cells UH672 and UH711. In both cases, the plots appear to result from three thermally activated, nonradiative recombination channels, labeled as α, β, and γ. The emission efficiency η can be therefore be described by

$$\eta=\left[1+\kappa^{\alpha}\exp\left(-\frac{E^{\alpha}}{k_BT}\right)+\kappa^{\beta}\exp\left(-\frac{E^{\beta}}{k_BT}\right)+\kappa^{\gamma}\exp\left(-\frac{E^{\gamma}}{k_BT}\right)\right]^{-1}, \tag{5}$$

where κ is the ratio of radiative to nonradiative recombination lifetimes for each recombination mechanisms at $T=300$ K, and E^{α}, E^{β}, and E^{γ} are their thermal activation energies. Fits of the CL data to Eq. (5) are shown in Fig. 7, and the fit parameters are given in Table III.

The shallow γ level ($E^{\gamma}=48$ meV) is common in both cells UH672 and UH711, and can be tentatively associated with an acceptor impurity. This is consistent with the suggestion of a *p*-type background doping in the intrinsic region that came out of the EBIC saturation regime analysis. The β level also has a similar energy and κ value for both InAsP wells. Since the well width is below 20 Å and the wells are relatively shallow ($\Delta E\sim 0.2$ eV) and since the β and γ defect levels appear to be insensitive to the As content, these defects could be within the barriers instead of within the wells. On the other hand, the characteristics of the defect level labeled α is sensitive to the As composition, suggesting that this defect level may reside within the wells. Due to the high efficiency of this level as a recombination channel (κ^{α} is relatively large), this near-midgap level is expected to be mainly responsible for the observed quantum well degradation.

TABLE III. Parameters determined from fits of integrated CL signal as a function of inverse temperature to Eq. (5). The data revealed three recombination channels, labeled α, β, γ. E^{α} is the defect level activation energy, κ is the ratio of the radiative to the nonradiative lifetime for each recombination channel.

	α		β		γ	
	E (eV)	κ	E (eV)	κ	E (meV)	κ
711	0.8	10^{21}	0.27	5×10^{7}	48	2×10^{12}
672	0.6	10^{16}	0.26	2×10^{7}	48	10^{2}

IV. DISCUSSION

The effect of proton-induced defects on the operational characteristics of solar cells can be incorporated into Anderson's ideal theory[4] by adding the contribution of the radiation-induced defects to the nonradiative recombination lifetime. Following Anderson, the J–V relation for a QWSC including nonradiative recombination is

$$J_{\mathrm{QW}}(V)=J_0(1+r_R\beta)\left[\exp\left(\frac{qV}{k_BT}\right)-1\right]-r_GJ_{\mathrm{SC}_B}+r_{\mathrm{NR}}qW\frac{\eta_{iB}}{\tau_{\mathrm{NRB}}}\left[\exp\left(\frac{qV}{2k_BT}\right)-1\right]. \quad (6)$$

In Eq. (6), the contribution of the nonradiative recombination to the current density is represented by the last term, where τ_{NRB} is the nonradiative lifetime in the barrier and n_{iB} is the carrier concentration in the barrier. The quantity, r_{NR}, is the nonradiative enhancement ratio, which models the contribution to the recombination current due to the radiation-induced traps, and is given by the following expression:

$$r_{\mathrm{NR}}=1+f_w\left[\gamma_{\mathrm{NR}}\gamma_{\mathrm{DOS}}\exp\left(\frac{\Delta E}{2k_BT}\right)-1\right]. \quad (7)$$

Similar to the oscillator enhancement factor, γ_B [see Eq. (2)], the term γ_{NR} is the lifetime reduction factor, which accounts for the difference in the non-radiative lifetimes in the wells and barriers ($\gamma_{\mathrm{NR}}=\tau_{\mathrm{NRB}}/\tau_{\mathrm{NRW}}$).

In a previous study of the radiation response of these cells,[12] the rate at which the open-circuit voltage degraded under proton irradiation was found to be higher for UH711 than UH672 for a 3 MeV proton fluence of 1×10^{13} cm^{-2}. At this fluence level, the V_{oc} of UH672 was approximately 20 mV higher than that of UH711. At higher proton fluences, quantum efficiency measurements showed that the thicker emitter of UH672 played a dominant role in the degradation mechanism of the cell. To estimate the contribution to the voltage drop due to nonradiative recombination enhancement within the wells, an expression of the rate of nonradiative recombination derived from the emission efficiency [Eq. (5)] can be used

$$R_{\mathrm{NR}}\propto\kappa^{\alpha}\exp[-E^a/k_BT]. \quad (8)$$

The ratio between the rates expressed by Eq. (8) for cells UH711 and UH672, yields a value between 1 and 50. The large range is due to the uncertainty of ±0.1 eV in the estimate of the energy of the α level. This result suggests that the nonradiative recombination rates are roughly equal in these cells. Therefore, the increased radiation sensitivity of V_{oc} in UH711 is more likely to be a result of the increased in InAsP well depth compared to cell UH672 instead of changes in the nonradiative lifetimes, as was discussed earlier in relation to Eq. (7).

The data presented here suggest that, given a similar base line cell structure, a QWSC with deeper wells will be more sensitive to irradiation than one with shallower wells. This is in good agreement with Anderson's ideal theory[4] where the introduction of a nonradiative recombination channel lowers V_{oc} more rapidly with increasing well depth. This effect seems to be a result of the radiation-induced, nonradiative recombination centers within the wells acting to lower the effective well gap, thus pushing the well gap below the ''deep-well'' limit where the QW efficiency enhancement become quenched. Indeed, the EBIC measurements showed that the capture of carriers in the wells was enhanced and the saturation regime at zero bias was not achieved after irradiation. Also, the increase in κ^{α} with higher As content suggests increased activity of the α level in cells with higher As concentrations.

It is worth noting that although both cells UH711 and UH672 were designed to provide nearly identical confined energy states in the quantum wells, the well thickness of cell UH711 was substantially smaller than that of cell UH672. As a result, the electron wave function of cell UH711 is expected to spread further into the barriers, hence, rendering the device more sensitive to effects in the barriers and at the well-barrier interfaces. Thus, the difference between the radiation response of the two cells may also be partly attributed to radiation-induced defects in the barrier region and to radiation-induced degradation of the well-barrier interface. In this case, it may be that the β defect level is also involved in the cell response, as it appears to be located in the barrier material.

V. SUMMARY AND CONCLUSIONS

An in-depth study of the carrier transport properties of InAsP/InP QWSCs using the techniques of EBIC and CL has been presented. Prior to irradiation, EBIC was used to analyze the saturation regime at the MQW region as a function of electric field strength, QW confinement energy, and excess carrier density. From the EBIC analysis, carrier lifetimes within the QWs have been estimated. Using the formalism of the ideal theory of Anderson,[4] these values were used to accurately model the measured V_{oc} of the QWSCs.

From EBIC measurements made on cells before and after proton irradiation, estimates of the base diffusion length degradation were made. It was found that radiation-induced recombination centers reduced the collection efficiency in the intrinsic regions. Analysis of the CL data taken in the irradiated cells revealed three nonradiative recombination levels. The effects of these radiation-induced defects on the QWSC performance was shown to be consistent with Anderson's theory when nonradiative recombination effects were included. The results suggest that for nearly identical quantum well confinement levels, the radiation hardness of a QWSC will decrease with an increase in As content and well depth, and a decrease in well thickness. This seems to be a result of radiation-induced defects acting as nonradiative recombination channels and possible well/barrier interface degradation.

ACKNOWLEDGMENTS

This work was supported in Spain by the CICYT (Comisión Interministerial de Ciencia y Tecnologia) under MAT94-0823-CO3-02 and by the Junta de Andalucia through TEP-0120. In the US, the work was supported at NRL by the U.S. Office of Naval Research. The work at the University of

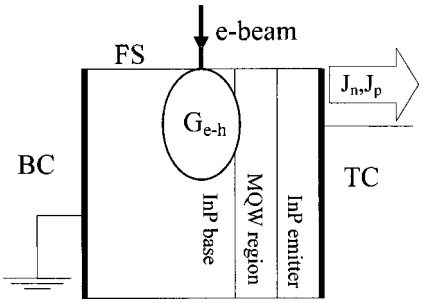

FIG. 8. The FEM is applied to solve the continuity equations for estimating the EBIC. This is illustrated here for a QWSC in the experimental arrangement.

Houston was in part sponsored through the Texas Advanced Research Program under Grant No. 003652-0094-1999.

APPENDIX

Extraction of the capture lifetime in the MQW region of QWSCs requires a detailed analysis of the EBIC. The finite element method (FEM) was applied to solve the Poisson equation

$$\nabla^2 V = -\frac{e}{\epsilon_s}(p-n+N) \tag{A1}$$

and the electron and hole current density equations

$$\begin{aligned} &\nabla \mathbf{J}_n = e(R-G), \mathbf{J}_n = e(-\mu_n n \nabla V + D_n \nabla n), \\ &\nabla \mathbf{J}_p = -e(R-G), \mathbf{J}_p = e(-\mu_p p \nabla V - D_p \nabla p) \end{aligned} \tag{A2}$$

for estimating the EBIC response. The rate of charge generation (G, $\mathrm{cm}^{-3}\,\mathrm{s}^{-1}$) in the continuity equations is the density of electron-hole pairs produced by the incident electron beam, whose spatial distribution has been previously estimated. The rate of recombination (R, $\mathrm{cm}^{-3}\,\mathrm{s}^{-1}$) has contributions from several mechanisms such as Shockley–Read–Hall and radiative recombination. The method is illustrated in Fig. 8. First, a FEM generator breaks down the QWSC into finite elements, whose properties can be defined in detail. Second, the rate of generation of electron-hole pairs is evaluated using a beam scattering model. In the measurements, the electron beam is scanned across the exposed surface of the QWSC and electron-hole pairs are produced underneath the incidence coordinate. Third, the continuity equations are solved for the boundary conditions applicable to the QWSC. In Fig. 8, the boundary conditions at the back and top contacts were established from both neutrality and equilibrium conditions, whereas for the free surface a Neumann condition was assumed, modified to take into account surface recombination. Solving the continuity equations, yields estimates of the current densities (J_n and J_p). These current densities correspond to the EBIC at the particular incidence coordinate. Moving the incidence coordinate of the beam in the code, enabled the EBIC to be calculated for a single scan.

The insertion of a MQW in the depletion region of a single junction solar cell has a major effect on the transport of excess carriers excited by the electron beam as they diffuse above the wells and are captured in the MQW region, or as carriers within the wells escape and are extracted by the electric field. Therefore, a specific rate equation rate for the MQW region needs to be included. The continuity equation was then modified in the QW region

$$G-R+\frac{1}{q}\nabla J = \int g(x,y,z)dV - \left[\frac{n^{\mathrm{QW}}}{\tau_R}+\frac{n^{\mathrm{QW}}}{\tau_{\mathrm{esc}}}-\frac{n^B}{\tau_{\mathrm{cap}}}\right] + \frac{1}{q}\nabla J = 0 \tag{A3}$$

and barriers

$$G-R+\frac{1}{q}\nabla J = \int g(x,y,z)dV - \left[\frac{n^B}{\tau_{R,\mathrm{bulk}}}+\frac{n^B}{\tau_{\mathrm{cap}}}\right] + \frac{1}{q}\nabla J = 0, \tag{A4}$$

where n^{QW} and n^B are the carrier densities within and above the wells, and τ_{esc} and τ_{cap} are the lifetimes for the escape of carriers from the wells and capture of carriers by the wells, respectively. For extraction of the carriers excited within the MQW region, the capture has to be minimized at the same time as escape from the wells has to be maximized. When the diffusion of carriers is restricted by capture at the MQW, a reduction of the EBIC signal is observed. Computing single scans at different capture lifetimes in Eqs. (A3) and (A4) and comparing them with the measurements, allows this parameter to be estimated.

[1] R. J. Walters, S. R. Messenger, H. L. Cotal, G. P. Summers, and E. A. Burke, Solid-State Electron. **39**, 797 (1996).
[2] R. J. Walters, S. R. Messenger, H. L. Cotal, M. A. Xapsos, S. J. Wojtczuk, H. B. Serreze, and G. P. Summers, J. Appl. Phys. **82**, 2164 (1997).
[3] K. W. Barnham, B. Braun, J. Nelson, M. Praxman, C. Button, J. S. Roberts, and C. T. Foxon, Appl. Phys. Lett. **59**, 135 (1991).
[4] N. G. Anderson, J. Appl. Phys. **78**, 1850 (1995).
[5] A. Freundlich, V. Rossignol, M. F. Vilela, and P. Renaud, Proc. IEEE First World Conference on Photovoltaic Energy Conversion, Wiakola, Hawaii, 1994, p. 1886.
[6] I. Serdiukova, C. Monier, M. F. Viela, and A. Freundlich, Appl. Phys. Lett. **74**, 2812 (1999).
[7] J. Nelson, I. Ballard, K. Barnham, J. P. Connolly, J. S. Roberts, and M. Pete, J. Appl. Phys. **86**, 5898 (1999).
[8] D. Araújo, M. J. Romero, F. Morier-Genoud, and R. Garcia, Mater. Sci. Eng., B **66**, 151 (1999).
[9] N. G. Anderson and S. J. Wojtczuk, J. Appl. Phys. **79**, 1973 (1996).
[10] R. J. Walters, G. P. Summers, S. R. Messsenger, A. Freundlich, C. Monier, and F. Newman, Prog. Photovoltaics **8**, 349 (2000).
[11] C. Monier, M. F. Vilela, I. Serdiukova, and A. Freundlich, Appl. Phys. Lett. **72**, 1587 (1998).
[12] R. J. Walters, G. P. Summers, A. Freundlich, C. Monier, M. Vilela, and S. R. Messenger, 2nd World Conference on Photovoltaic Energy Conversion, Vienna, Austria, 1998, p. 3723.